

7

Microfabricated atomic magnetometers

S. Knappe and J. Kitching

82d6a1d6f339aa274f6f257c38cec619
ebrary

7.1 Introduction

In this chapter, we discuss miniaturized atomic magnetometers, and the technology and applications relevant to this somewhat unusual direction in magnetometer research and development [1]. By “miniaturized,” we mean, in addition to their small size, magnetometers that have associated desirable qualities such as low power consumption, low cost, high reliability, and the potential for mass fabrication. Together with the high sensitivity usually obtained from the use of atoms, these properties result in magnetic sensors that fill a unique application space and may in fact enable new applications for which atomic magnetometers have not before been used.

It is perhaps surprising that atomic magnetometers in general are not more widely used in the world today. The main application areas at present are geophysical surveying and magnetic anomaly detection. Geophysical surveying is important in oil and mineral exploration, archeology, and unexploded ordnance detection and is typically carried out by moving one or more atomic magnetometers over the area to be surveyed. The magnetic “map” generated from this data can show the locations and in some cases the size and shape of magnetic objects or structures buried beneath the surface of the earth. Magnetic anomalies include vehicles, ships, and submarines and are typically detected via magnetic gradiometry. There are, however, only three major companies in North America, employing perhaps a few hundred people, that manufacture and sell atomic magnetometers. This effort represents a rather small fraction of the worldwide yearly market for magnetic sensors, which was estimated in 2005 to be about \$1 billion [2]. Commercial atomic magnetometers are described in Chapter 20.

One major impediment to more widespread use of atomic magnetometers is their high cost and instrumental complexity relative to other types of magnetic sensor technology. Hall

Optical Magnetometry, ed. Budker, D. and Jackson Kimball, D. F. Published by Cambridge University Press.
© Cambridge University Press 2013.

82d6a1d6f339aa274f6f257c38cec619
ebrary

probes and magnetoresistive sensors, for example, have captured the bulk of the magnetometer market share mainly because they are manufactured as low-cost integrated circuits that can be integrated as electronic components into automobiles and other consumer or industrial products. Thus miniaturization and associated low-power operation and low-cost production are critical factors in determining whether a technology achieves commercial success and widespread use in real-world applications.

This sentiment is a key driving force behind our work, and the work of others, to develop highly miniaturized atomic magnetometers. Research in the field of atomic magnetometers has traditionally focused largely on sensitivity and the underlying physics that determines this aspect of the performance of magnetic sensors. However, the development of novel fabrication techniques that enable a high degree of miniaturization may be as important in determining how atomic magnetometers are used.

We discuss here work that was initiated at NIST in 2004 as an offshoot of a program to develop highly miniaturized “chip-scale” atomic clocks [3]. We begin with an analysis of how the sensitivity of a vapor-cell magnetic sensor scales with the size of the cell under certain reasonable assumptions about how the sensor is operated. We then discuss aspects of the design and fabrication of chip-scale atomic magnetometers with emphasis on the use of micromachining processes. We conclude with a discussion of applications of chip-scale atomic magnetometers, and in particular focus on biomagnetic imaging and the detection of nuclear magnetic resonance.

7.2 Sensitivity scaling with size

The sensitivity of an atomic magnetometer based on N uncorrelated atoms is limited fundamentally by quantum projection noise in the measurement of individual atomic spins. Under these conditions, the sensitivity can be written as (see Ref. [4] as well as Chapter 1, Section 1.1.1, and Chapter 2):

$$\delta B = \frac{1}{\gamma} \frac{1}{\sqrt{N\tau T}}, \quad (7.1)$$

where γ is the atom’s gyromagnetic ratio, τ is the atom relaxation time, and T is the measurement period. We consider here how the sensitivity scales with the size of the vapor cell. The cell size influences the sensitivity in two main ways: through the relaxation time τ and through the atom number N . The atom number is clearly determined by the alkali vapor density n_{Al} and the cell volume V as

$$N = n_{\text{Al}} V. \quad (7.2)$$

In the limit of high alkali atom density, where the relaxation time is dominated by collisions of alkali atoms with other alkali atoms, the relaxation time can be written

$$\tau_{\text{Al-Al}} \approx \frac{1}{n_{\text{Al}} \sigma_{\text{col}} v}, \quad (7.3)$$

where σ_{col} is the collision cross-section and v is the mean relative velocity of the atoms. Under these conditions, the field sensitivity is given by [5]

$$\delta B \approx \frac{1}{\gamma} \sqrt{\frac{\sigma_{\text{col}} v}{VT}}, \quad (7.4)$$

and scales as the inverse one-half power of the cell volume. When spin-exchange collisions dominate the relaxation rate, $\sigma_{\text{col}} \approx \sigma_{\text{se}}$, and the sensitivity scales with cell dimension approximately as $1 \text{ fT}/\sqrt{\text{Hz} \cdot \text{cm}^3}$ for alkali atoms, where the spin-exchange collision cross-section is about $2 \times 10^{-14} \text{ cm}^2$. Under some circumstances the effects of spin-exchange collisions can be suppressed [6, 7], in which case weaker spin-destruction processes dominate. In this case the collision cross-section can be as low as $2 \times 10^{-18} \text{ cm}^2$ for ^{39}K , and a sensitivity near $10 \text{ aT}/\sqrt{\text{Hz}}$ may be possible in a cell 1 cm in size.

The above analysis assumes relaxation dominated by alkali-alkali collisions. However, additional relaxation processes are also usually present. These processes include collisions with the cell walls, collisions with buffer-gas atoms if a buffer gas is present, and relaxation due to magnetic field gradients. These other processes do not depend on the alkali atom density but do, in general, depend directly or indirectly on the cell volume. We may therefore write

$$\frac{1}{\tau} = \frac{1}{\tau_{\text{bg}}} + \frac{1}{\tau_w} + \frac{1}{\tau_{\text{oth}}} + \frac{1}{\tau_{\text{Al-Al}}}, \quad (7.5)$$

where the wall-induced relaxation rate, $1/\tau_w$, depends on the cell volume, the buffer-gas-induced relaxation rate is $1/\tau_{\text{bg}}$, and the relaxation due to other processes, $1/\tau_{\text{oth}}$, can be made small with appropriate environmental controls. As discussed below, the buffer-gas pressure is usually adjusted to minimize the relaxation rate for a given cell volume, and is hence indirectly dependent on this parameter.

In an otherwise evacuated cell containing alkali atoms, the atom density is typically small enough that the atoms fly ballistically between wall collisions. Since a single collision with an uncoated glass wall depolarizes an atom completely, the relaxation time is roughly equal to the transit time across the cell and is on the order of 30 ms for a cell with a characteristic size of 1 cm. Wall coatings such as paraffin are known to lengthen considerably the wall-collisional relaxation time (see Chapter 11); typically a thousand wall collisions or more are obtained before the atoms relax [8], although recent results have indicated the possibility that some unique coatings may allow considerably more bounces [9]. In either case the wall-collision-induced relaxation rate can be written as $1/\tau_w = \alpha v/L$, where α is the depolarization probability for one collision and $L \sim V^{1/3}$ is the characteristic size of the cell. Highly miniaturized glass-blown vapor cells with high-quality wall coatings have been recently demonstrated [10].

Buffer gases can also be used to reduce wall-induced relaxation by forcing the alkali atoms to diffuse through the cell and therefore collide with the walls less often. In this case, the relaxation rate is a balance between the diffusion-mediated wall collisions and

the relaxation due to collisions with the buffer-gas atoms themselves [11]. Since the wall-related component is inversely proportional to the buffer-gas pressure, while the buffer-gas relaxation is proportional to this quantity, an optimal buffer-gas pressure exists for a given cell size that minimizes the relaxation. At the optimum buffer-gas pressure, the combined relaxation rate due to buffer gas and walls is equal to

$$\frac{1}{\tau_{\text{bg}}} + \frac{1}{\tau_w} = 2 \frac{\sqrt{D_0 \gamma_0}}{\beta L}, \quad (7.6)$$

where D_0 is the diffusion constant and γ_0 is the buffer-gas-induced relaxation rate, both at a buffer-gas density of 1 amagat, and β is a constant of order unity that depends on the cell geometry. We do not consider the effect of nuclear slow-down factors on relaxation here.

We therefore find that both a wall-coated cell and a cell containing a buffer gas whose pressure is optimized for the size of the cell generate relaxation rates that are inversely proportional to the linear dimension of the cell. In fact, for most of the commonly used wall coatings and buffer gases, the coefficients relating the cell size to the relaxation time are quite similar and approximately equal to $2\pi \times 100 \text{ Hz} \cdot \text{mm}$.

At low cell temperatures, where the alkali-alkali collisions do not contribute to the linewidth, the magnetometer sensitivity improves as the alkali density (cell temperature) is increased because of the improved signal-to-noise ratio. When alkali-alkali collisions dominate the linewidth at high cell temperatures, any gains in sensitivity due to improved signal-to-noise are offset by a broader resonance linewidth. The best operating point therefore occurs when the relaxation due to alkali-alkali collisions is approximately equal to the relaxation due to other processes. These processes are collisions with the cell walls and buffer-gas atoms, if a buffer gas is present, and the relaxation time scales linearly with the cell size under optimal conditions [12]. Figure 7.1(a), adapted from Shah *et al.* [1], shows the magnetometer sensitivity as a function of cell size assuming the linewidth is optimized at each cell size as above and assuming spin projection as the dominant noise source. We also assume two different relaxation regimes: one in which spin-exchange collisions dominate (lines labeled A) and another in which spin-exchange relaxation is suppressed and spin-destruction relaxation dominates (lines labeled B). Spin-exchange-relaxation-free (SERF) magnetometry, corresponding to the latter case (B lines), is discussed in Chapter 5. Clearly better sensitivity is obtained at a given cell size when spin-exchange relaxation is suppressed. This is because higher cell temperatures can be used in this case without broadening the natural cell linewidth, and hence more atoms can be interrogated, resulting in a higher signal-to-noise ratio. The difference in sensitivity between atoms of different species at a given cell size is determined almost entirely by the difference in collision cross-sections.

The analysis in Fig. 7.1(a) assumes spin projection as the only noise source. A number of noise contributions other than spin projection noise are also present in atomic magnetometers. These include photon shot noise, light-shift noise, laser intensity noise, and frequency-to-amplitude conversion noise. The effects of these noise terms on the sensitivity of atomic magnetometers can be evaluated somewhat heuristically by describing them

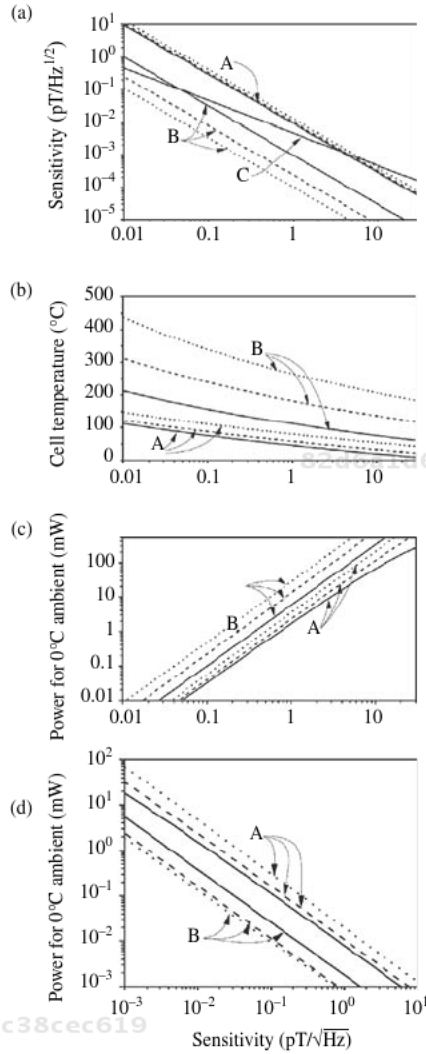


Figure 7.1 (Adapted from Ref. [1].) Scaling of magnetometer parameters: (a) sensitivity, (b) cell temperature, and (c) power as a function of size. (d) Electrical power required to reach a given sensitivity, under assumptions outlined in the text. Traces A and B show the scaling for linewidths limited by spin-exchange collisions and spin-destruction collisions, respectively. Solid lines refer to Cs, dashed lines to ⁸⁷Rb, and dotted lines to ³⁹K. Solid line C in plot (a) refers to a signal-to-noise ratio of $5 \times 10^6 \sqrt{\text{Hz}}$.

in terms of a detection signal-to-noise ratio (S/N), which limits how well the center of the magnetic resonance can be determined. Photon shot noise on 1 mW of light results in a S/N of $5 \times 10^7 \sqrt{\text{Hz}}$. In practice, a S/N between 10^4 and 10^5 at one second can be achieved without too much difficulty, although a S/N as high as $\sim 2 \times 10^7 \sqrt{\text{Hz}}$ has been achieved

in some experiments [13]. The solid line C in Fig. 7.1(a) shows the expected sensitivity as a function of cell size for a fixed S/N of $5 \times 10^6 \sqrt{\text{Hz}}$ for typical buffer-gas vapor cells.

In practice, it seems reasonable that alkali vapor cells could be produced ranging in size from a few centimeters down to about $10 \mu\text{m}$. Over this size range, the fundamental magnetometer sensitivity may vary from a few $\text{aT}/\sqrt{\text{Hz}}$ for the largest cells to a few $\text{pT}/\sqrt{\text{Hz}}$ for the smallest. This scaling implies an interesting and important technical trade-off between sensitivity and size, particularly when considering instrumentation for use in real-world applications. By making their vapor cells larger, atomic magnetometers can certainly be made more sensitive, but with loss of overall utility, and ultimately value, due to the bulkiness of the apparatus. The value of high sensitivity is compromised even further when considering magnetic noise that is present in all shielded and unshielded environments. Field fluctuations of geomagnetic origin, for example, have a magnitude of about $1 \text{ pT}/\sqrt{\text{Hz}}$ at 1 Hz, while thermal noise from magnetic shields is approximately a few $\text{fT}/\sqrt{\text{Hz}}$ for shield diameters of about 1 m. For biomagnetic imaging, the finite conductance of the human body generates magnetic noise at a level of a fraction of a $\text{fT}/\sqrt{\text{Hz}}$. Even though gradiometry can be used in some cases, the benefits of improving the magnetometer sensitivity are therefore substantially reduced once the femtotesla regime is reached. From a purely instrument engineering perspective, this viewpoint motivates the development of very small magnetometers, which trade off high sensitivity for low power, ease of fabrication and operation, and low cost.

The optimal sensitivity in Fig. 7.1(a) is reached only when the relaxation rate is dominated by alkali–alkali collisions. Since the alkali density, and hence the relaxation rate, is determined by the cell temperature, the curves in Fig. 7.1(a) define a minimum temperature at which the cell must operate to achieve the desired sensitivity. The optimal alkali density is

$$n_{\text{Al}} = \frac{2\sqrt{D_0\gamma_0}}{\beta L \sigma_{\text{col}} v}, \quad (7.7)$$

and the cell temperature required to achieve this density is plotted in Fig. 7.1(b). Even for rather small cells, approaching $10 \mu\text{m}$ in size, the required temperatures are practical to achieve, at least for ^{87}Rb and Cs . Cesium begins diffusing rapidly into Pyrex at temperatures near 350°C , and operation of a Pyrex cell containing Cs is not practical above that temperature.

Finally, it is possible to estimate the power required to heat the cell to its operating temperature. We assume here that the cell can be thermally isolated from the environment to a point where radiation is the dominant source of heat loss. Using the Stefan–Boltzmann law, and assuming a surface emissivity of unity, the power required to maintain the cell temperature in a 0°C ambient is shown in Fig. 7.1(c) as a function of cell size. The results of Fig. 7.1(a) and Fig. 7.1(c) can be combined to determine how much power is required to reach a given sensitivity level. This is plotted in Fig. 7.1(d). Clearly, higher sensitivity requires more power. However, sensitivities near $1 \text{ pT}/\sqrt{\text{Hz}}$ can in principle be achieved with far less than 1 mW of heating power, suggesting that moderately sensitive but highly autonomous battery-operated sensors are possible. While the electronics required to control

such a sensor must be made to operate on comparably little power, it is likely that this could be achieved with moderate investment in an appropriate low-power application-specific integrated circuit.

7.3 Sensor fabrication

The design and fabrication of atomic magnetometers with millimeter-scale dimensions has presented a number of interesting challenges over the last decade. Research on this topic grew out of previous work to develop chip-scale atomic clocks [3, 12] and many of the elements of the two types of instruments are similar. In fact, the first chip-scale atomic magnetometer to be operated was the same device as an earlier chip-scale atomic clock.

The main components of an optical magnetometer physics package are the following: a light source, a vapor cell, optics to direct and polarize the light, heaters to heat the vapor cell, and photodetectors. In conventional commercial alkali magnetometers an alkali lamp excited with an RF discharge is used as the light source. The vapor cell is fabricated by use of glass-blowing techniques and contains the alkali-metal atoms and a buffer gas to reduce the effects of wall collisions as described above. Commercial atomic magnetometers have a sensor volume of approximately 1 L and require about 10 W of electrical power to operate.

Highly miniaturized versions of these instruments have incorporated two main improvements: the first is to use a low-power semiconductor laser as the light source. The RF discharges needed to activate the lamp require 1 W of electrical power or more to operate. Lasers, on the other hand, are considerably more efficient. Vertical-cavity surface emitting lasers (VCSELs), for example, can have a wall-plug efficiency above 10% and can therefore run on a few milliwatts of electrical power. The second improvement is the use of microfabricated alkali vapor cells, which allow the alkali atoms to be contained in a much smaller volume than is achieved with glass-blown cells. The smaller cell size in turn allows the power needed to heat the cell to its operating temperature to be much lower. These two improvements, along with a number of more minor changes, have allowed the demonstration of atomic magnetometer sensor heads with volumes below 10 mm³, as well as some novel designs that are outlined below.

To address applications with different requirements, two generally different approaches to miniaturization have been tried: a fully integrated chip-scale magnetic sensor and microfabricated remote sensor heads fiber-optically coupled to a central control unit.

The first approach to miniaturization of optical magnetometers closely followed that developed for chip-scale atomic clocks. The goal of this design, in addition to small size and low power, was to allow for wafer-level fabrication and assembly in order to make parallel fabrication of large numbers possible at reasonable cost. Figure 7.2 shows a photograph of one of the first chip-scale atomic magnetometer physics packages, as well as a sketch of the separate components. The physics package, based on the standard M_x configuration (see Chapter 4) and pumped on the D1 line of ⁸⁷Rb at 795 nm, had a total volume of 25 mm³ and required about 200 mW at an ambient temperature near room temperature. The device housed a VCSEL bonded to the bottom baseplate that created the light tuned to the D1

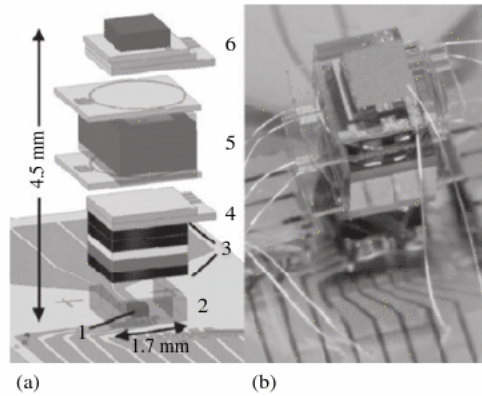


Figure 7.2 (Adapted from Ref. [14].) (a) Design and (b) photograph of a chip-scale atomic magnetometer. A laser (1), surrounded by a spacer (2), emits light through some optics (3) to illuminate a vapor cell (5); the light is detected with a photodiode (6). Ohmic heaters (4) are used to heat the cell.

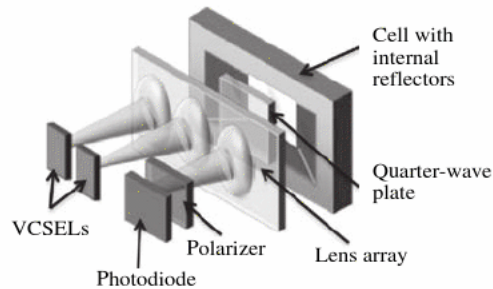


Figure 7.3 Reflectors internal to the cell can be used to redirect laser beams and create perpendicular pump/probe geometries.

transition of ^{87}Rb to optically pump the atoms and probe the precessing atomic spins. The light emitted from the laser was detected by the photodiode on top of the stack, after it was attenuated, collimated, circularly polarized and transmitted through an alkali vapor cell. The cell was heated to 90°C by two heaters on either side of the cell, to achieve an optical depth of 0.7 on resonance. Two H-field coils were added to create an oscillating field parallel to the laser beam. Electrical connections were made through wire bonds to the baseplate. More complicated MEMS designs for multibeam geometries have been proposed. One of them, as shown in Fig. 7.3, uses vapor cells with internal reflectors, and dielectric coatings applied on angled surfaces inside the cell [15]. Another design simply tilted the cell at an angle of 45° [1, 16]. A third design used a diverging laser beam to optically pump and probe atoms within the same cell in two different directions [17].

While this type of design enables inexpensive fabrication of many individual physics packages, the proximity of the laser and many electrical connections to the detection volume

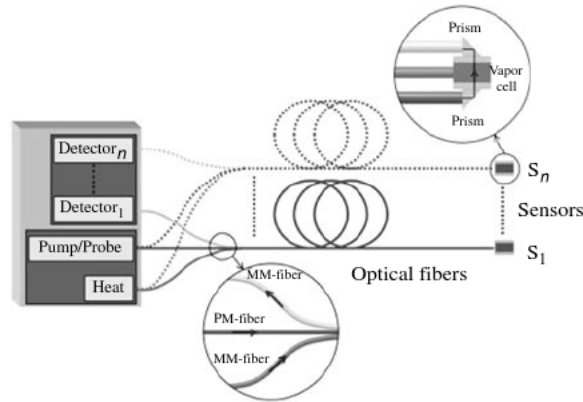


Figure 7.4 Concept of fiber-optically coupled magnetometer array. A series of sensor heads ($S_1 - S_n$) is coupled fiber-optically to a common control unit containing a pump/probe laser, a heating laser, and a series of photodetectors.

inside the cell limited the sensitivity and generated spurious magnetic field signals. It can therefore be advantageous to separate the laser and detector from the vapor cell and couple the light to and from the cell either through optical fibers or through free space. This approach can be especially attractive when large sensor arrays are desirable, so that all sensor heads can be interrogated with the same laser. A sketch of such a magnetometer is shown in Fig. 7.4. Because light from the laser is distributed among many sensor heads, a higher-power laser can be used with better noise characteristics compared to those of VCSELs.

In all of these approaches, care has to be taken that the materials used for the sensors generate no magnetic fields. While this sounds trivial, it must be kept in mind that any conductive material near the sensor volume is a source of magnetic noise through the thermal motion of electrons [18, 19]. Lee and Romalis [20] calculated the noise from high-permeability magnetic shielding and suggested the use of ferrite shields. Furthermore, Griffith *et al.* [21] calculated the noise expected from cell bodies made from high-conductivity silicon to be a few fT/\sqrt{Hz} . By using silicon materials with lower conductivity, this noise can be reduced to below $1 fT/\sqrt{Hz}$. Furthermore, when the noise in a cell with solid Rb on the cell walls was measured and compared to one with minimal amounts of solid Rb present, a difference of several fT/\sqrt{Hz} was found. This suggests that the presence of the Rb on the walls of such a small cell contributes significantly to the sensor noise [21].

7.4 Vapor cells

Until now, all microfabricated optical magnetometers have used micromachined alkali vapor cells. Bulk etching techniques in silicon allow for precisely defined cell geometries with the possibility of thin channels and alkali reservoirs with precision better than $25 \mu m$. Wafer thicknesses ranging from $300 \mu m$ to $3 mm$ have been used and cells with lateral dimensions

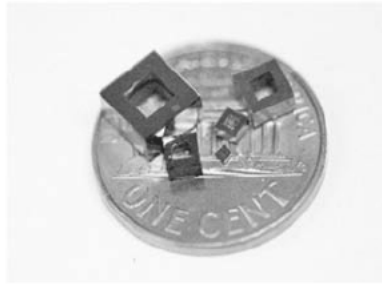


Figure 7.5 A variety of microfabricated alkali vapor cells, showing a range of interior dimension from 4 mm to 0.5 mm.

between 100 μm and 5 mm have been demonstrated. The two main etching options that have been explored are the dry method of deep reactive ion etching (DRIE) and the wet etch with potassium hydroxide (KOH) [22]. Some other means of creating cell cavities such as ultrasonic drilling and diamond mechanical drilling have also been successful. A number of microfabricated vapor cells of different sizes are shown in Fig. 7.5.

While silicon microfabrication methods are already well established, the main new challenge in fabricating the vapor cell lies in the filling method. Many different approaches for filling MEMS vapor cells have been attempted for the development of chip-scale atomic clocks [23]. While microfabricated atomic magnetometer cells have slightly different driving requirements compared to those for a clock, many challenges are the same. The most common method of filling cells with alkali atoms takes advantage of anodic bonding [24] of borosilicate glass windows onto the silicon body. This method creates a permanent electrostatic bond between the glass and silicon. An initial bond between the silicon frame and the glass on one side of the cell is usually performed in air. This “preform” is then transferred to a glove box or a vacuum chamber in order to minimize the oxygen or water content in the cell. After deposition of the alkali atoms, the chamber is backfilled with a buffer gas and a second glass wafer is bonded on the other side of the silicon. While the most common buffer gas inside the cells is nitrogen, cells have also been made with neon, argon, helium, hydrogen, and xenon. The actual filling of the cell inside the chamber is often done by creating an atomic beam of alkali atoms that passes through an aperture into the bottom of the cell, where the atoms condense [25]. In a final step, the wafers or wafer chips are diced to form the actual vapor cells. Figure 7.5 shows a variety of such cells.

7.5 Heating and thermal management

Another challenge is maintaining an elevated cell temperature with low electrical power. The short path lengths of the microfabricated cells require that the cell is heated to increase the alkali vapor pressure. For a 1 mm long Rb cell with 1 amagat of nitrogen, a temperature of 150°C is required to obtain an optical density of 5 on resonance. When using electrical

heating with resistive films, the disturbance of the atoms from stray magnetic fields should be minimized. First, the heater currents can be modulated at a frequency much higher than the bandwidth of the magnetometer. Alternatively, the currents could be chopped, and measurements taken only when the currents are off. Second, the heater traces can be patterned in such a way that the generated fields are largely canceled. This can be done within the same heater layer and also by use of two heater films with a thin isolating layer in between. This was implemented, for example, by Schwindt *et al.* [14], who used patterned transparent indium–tin–oxide (ITO) traces and a 2 μm thick insulating layer of benzocyclobutene. Mhaskar *et al.* [26] deposited titanium traces with an insulating layer of SU-8.

Magnetic fields induced by heating currents can be eliminated entirely through the use of optical heating. Preusser *et al.* [27] demonstrated a fiber-coupled sensor head that was heated by 915 nm light that was absorbed by the body of the vapor cell. While this was demonstrated in a fiber-coupled system, optical heating allows for the possibility of truly remote sensor heads, where all connections to the central control unit are made with light beams through free space [27].

Finally, in order to minimize the power required for maintaining the cell temperature, good thermal insulation is needed. One option is to suspend the cell in a web of strained polyimide inside a vacuum enclosure, a technology pioneered for chip-scale atomic devices by Mescher *et al.* [28, 29]. They were able to stabilize the temperature of a (1.5 mm)³ vapor cell to 75°C with a total power of less than 10 mW, limited by radiation from the cell surface. Other approaches used silicon [30, 31] or silicon nitride [32] as materials for the suspensions. Finally, alternative methods to vacuum packaging and for radiation shielding have been implemented in slightly larger optical magnetometers. They include packaging with aerogel [33] and patterned gold reflectors [34].

7.6 Performance

The sensitivity of microfabricated atomic magnetometers has improved from the level of 40 pT/ $\sqrt{\text{Hz}}$ in 2004 for an integrated device to 5 fT/ $\sqrt{\text{Hz}}$ in 2010 measured in a table-top experiment. The sensitivity of a variety of magnetometers is plotted in Fig. 7.6. Traces A and B are the measured sensitivity of devices for which the laser, optics, and photodetector are integrated together as shown in Fig. 7.2. Traces C and D are measurements carried out in microfabricated vapor cells, but with table-top optics, which allows a high degree of flexibility in the experimental parameters and hence easier optimization. These last traces therefore give an estimate of what sensitivity is possible in a microfabricated cell.

In the frequency band between 20 Hz and 200 Hz, the best sensitivities measured to date are ~ 5 fT/ $\sqrt{\text{Hz}}$. This is quite competitive with commercial SQUID-based magnetometers, but of course atomic magnetometers have the considerable advantage that there is no need for cooling of the sensor to cryogenic temperatures. At frequencies below 10 Hz, most of the microfabricated sensors show increasing noise, although careful measurements have been carried out in only a few cases. In some cases, the low-frequency noise has been

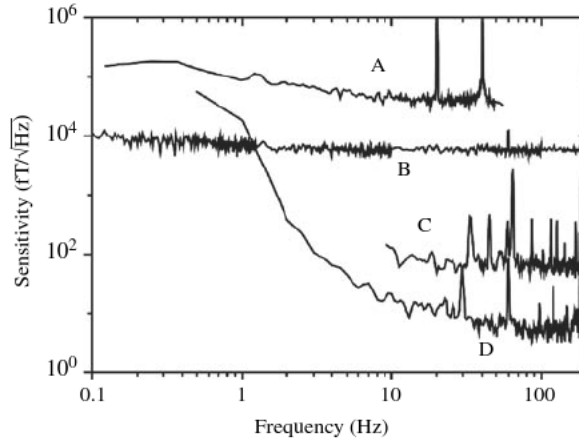


Figure 7.6 Sensitivity of microfabricated atomic magnetometers. (A) Integrated coherent population trapping magnetometer (Schwindt *et al.* [35]), (B) integrated M_x magnetometer (Schwindt *et al.* [14]), (C) SERF magnetometer in microfabricated vapor cell (Shah *et al.* [1]), (D) advanced SERF magnetometer in microfabricated vapor cell (from Griffith *et al.* [21]).

associated with variations of the current flowing through the resistive heaters [26] caused, for example, by time-varying changes in the properties of the heater material. At present, it is not believed that the low-frequency component is a fundamental property of the magnetic sensors.

The bandwidth of microfabricated atomic magnetometers is limited in most cases by the width of the resonance line. Because the resonance width increases as the size of the cell is decreased, highly miniaturized sensors have a natural advantage over their larger counterparts for the measurement of higher-frequency signals: while the larger linewidth (due to more frequent wall collisions) results in worse sensitivity, it simultaneously results in a wider frequency band over which fields can be measured with the same signal-to-noise ratio. The width of this band is important in particular for biomagnetic measurements, for which signals exist from 1 Hz to 100 Hz. Microfabricated atomic magnetometers have demonstrated sensitivities of $6 \text{ pT}/\sqrt{\text{Hz}}$ in the M_x mode with a bandwidth of 1 kHz [14], and $5 \text{ fT}/\sqrt{\text{Hz}}$ in the SERF mode with a bandwidth of 200 Hz [21]. The bandwidth associated with the highest-sensitivity instruments is still largely compatible with many biomagnetic applications.

The dynamic range of microfabricated atomic magnetometers is determined by essentially the same considerations as for larger sensors. When operating in the M_x spin-precession mode, the lowest field that can be measured is determined by the resonance linewidth, which is approximately 500 nT for a cell of interior dimension $\sim 1 \text{ mm}$. Very high magnetic fields can in principle be measured with these sensors, although some instrumentation complications arise at high fields due to the nonlinear Zeeman shift (see Chapter 1) and the large range of drive oscillator frequencies.

In the SERF operating mode, the lowest measurable field is determined by the fundamental sensitivity of the magnetometer. The highest measurable field is determined by the linearity of the resonance slope. For the sensor of Griffith *et al.* [21], for which the resonance width is about 200 Hz, this is about 50 nT. By using field-nulling coils that are actively adjusted to produce zero field at the sensor location, much higher dynamic ranges should be possible.

The heading error of a scalar sensor refers to the change in the sensor reading as the sensor axis is rotated with respect to the field to be measured. Heading errors are generated by a number of effects. Two leading causes are the nonlinear Zeeman shift described above and misalignment of the light propagation axis with the axis of the RF coils [36]. The magnitude of the nonlinear Zeeman shift does not depend on the width of the resonance line and the heading errors due to this effect are therefore expected to be similar in magnitude to those of larger sensors, at least for ^{133}Cs and ^{87}Rb , where the splitting (in Earth's field) is much smaller than the resonance width for both types of magnetometers. Misalignment of the field-coil axis with the light-propagation axis generates a heading error that scales with the resonance width and hence is more important for microfabricated magnetometers than it is for larger sensors.

7.7 Applications of microfabricated magnetometers

As mentioned in the introduction, the main advantages of microfabricated atomic magnetometers over larger sensors are their small size, low power requirements, and potential low fabrication cost. These advantages come at the cost of reduced sensitivity, and hence the applications for which microfabricated atomic magnetometers will be most important are those that have a specific need for microfabricated magnetometers' intrinsic strengths.

Remote detection of magnetic anomalies is one area where low power and low cost may offer considerable advantage. All commercial atomic magnetometers developed to date require several watts of power to run. This essentially prohibits remote, battery-powered operation for extended periods. Microfabricated atomic magnetometers offer the possibility of moderate sensitivity ($\sim 100 \text{ fT}/\sqrt{\text{Hz}}$), while requiring only a few milliwatts of power [see Fig. 7.1(d)]. Li-ion batteries have an energy density of about $0.5 \text{ Wh}/\text{cm}^3$. Thus, a 1 cm^3 battery could power a microfabricated atomic magnetometer for a month or more. Hence, remote operation of a microfabricated atomic magnetometer is feasible within the constraints of the determining physics. One could imagine deploying large numbers of these sensors along a perimeter to detect ships, submarines, or vehicles.

A second major application is the detection of magnetic signals generated by the human body. While many parts of the body produce magnetic fields, the two most important are the heart and the brain. These organs generate fields with strengths of about 100 pT outside the chest, and 1 pT outside the head, respectively. To measure these fields, with reasonable signal-to-noise ratio, sensors with sensitivities in the $\text{fT}/\sqrt{\text{Hz}}$ range are needed. Traditionally, measurements of these fields have been limited to SQUID-based magnetic sensors, since only these have had the required sensitivity. However, both large-scale atomic

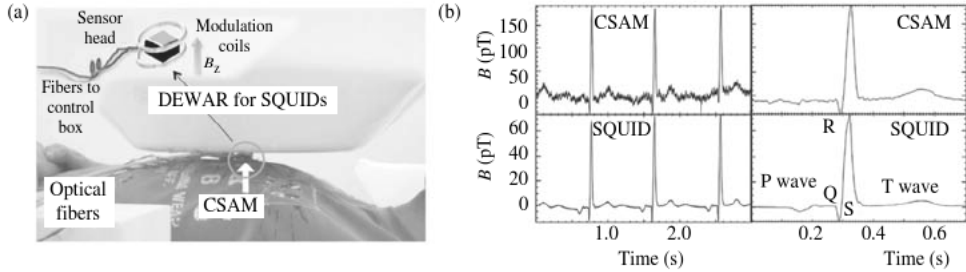


Figure 7.7 (From Knappe *et al.* [40]. Copyright 2010, American Institute of Physics.) Measurement of the magnetic field from a human heart by use of a microfabricated atomic magnetometer. (a) Experimental setup showing a microfabricated atomic magnetometer (CSAM) positioned below a SQUID dewar. (b) Measurements were made simultaneously with a SQUID sensor for comparison.

82d6a1d6f339aa274f6f257c38cec619
ebrary

magnetometers [37–39] and more recently microfabricated atomic magnetometers [40] have been shown to be capable of measuring one or both of these biomagnetic sources. A photograph of an experiment comparing a microfabricated atomic magnetometer to a SQUID-based biomagnetic system is shown in Fig. 7.7(a); signals from a human heart are shown in Fig. 7.7(b).

A third application of microfabricated atomic magnetometers is in low-field nuclear magnetic resonance (NMR). Traditional NMR requires large magnetic fields to (a) polarize the nuclei in the sample and (b) create a nuclear resonance frequency high enough to be detected with high sensitivity by an inductive pick-up coil. Magnetometers with high sensitivity at low frequencies (DC, essentially) are an enabling component for some types of low-field NMR. While SQUID magnetometers have been used [41], there is growing interest in using instead atomic magnetometers [42] due to the lack of need for low-temperature cooling. Microfabricated atomic magnetometers offer an additional advantage in that they could be integrated into portable hand-held instruments for remote imaging [43] or chemical species identification [44].

82d6a1d6f339aa274f6f257c38cec619
ebrary

A basic demonstration of the detection of nuclear magnetization was made by Ledbetter *et al.* [45]. In this experiment, shown schematically in Fig. 7.8(a), hydrogen nuclei (protons) in water were weakly polarized in a permanent magnet; the water then flowed into a microfluidic chip that included a microfabricated vapor cell, inside a shielded environment. The polarized nuclei produced a weak magnetic field that was comparable to the residual magnetic field from the magnetic shields. The orientation of the nuclear polarization was flipped using standard nuclear spin manipulation techniques and the resulting quasi-static change in the magnetic field that occurred as the reoriented atoms flowed into the microfluidic channel was measured, as shown in Fig. 7.8(b). The magnitude of this field change was about 20 pT and was easily detectable by use of the microfabricated atomic magnetometer.

Subsequent experiments have shown that intramolecular J -coupling can be detected at zero magnetic field with microfabricated vapor cells [46], allowing the identification of chemical species without relying on the chemical shift that occurs only at high magnetic

82d6a1d6f339aa274f6f257c38cec619
ebrary

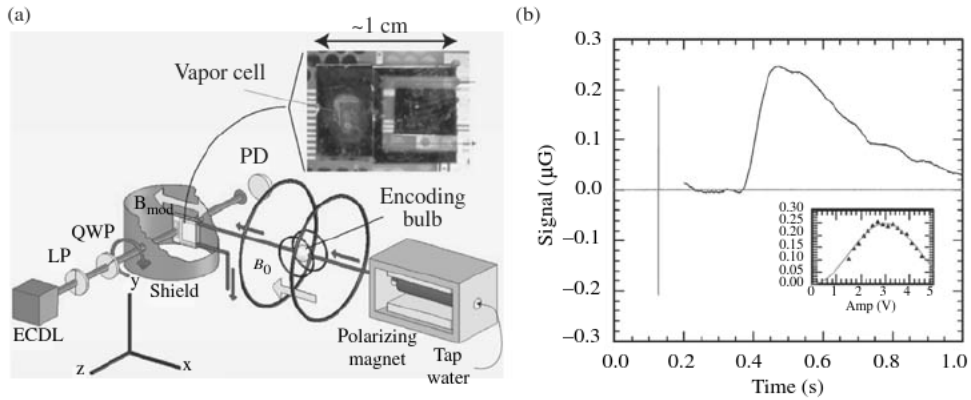


Figure 7.8 (From Ledbetter *et al.* [45].) Measurement of weak nuclear polarization in water by use of a microfabricated atomic magnetometer. (a) Experimental setup showing tap water running through a polarizing magnet and onto the NMR detection chip. (b) Change in the signal observed by the magnetometer after application of a π -pulse in the encoding bulb at the time indicated by the vertical line.

fields. Finally, an enhancement of the nuclear polarization by use of parahydrogen in an experiment with atomic-micromagnetometer detection was demonstrated by Theis *et al.* [47], leading to substantially enhanced magnetic resonance signals.

We anticipate that microfabricated atomic magnetometers will find a number of additional applications, including the measurement of magnetic fields in space and detection of magnetic micro- and nano-particles [40, 48].

7.8 Outlook

This chapter has reviewed recent work to develop highly miniaturized atomic magnetometers. The core technical element is the use of microfabricated alkali vapor cells, which allow the atoms to be confined in volumes below 1 mm^3 . These cells can be integrated into sensor heads with volumes as small as 20 mm^3 , and can achieve sensitivities as low as $5 \text{ fT}/\sqrt{\text{Hz}}$.

We anticipate three future directions for the development of this technology. First, improved sensitivity is always of value, and millimeter-scale sensors are not yet reaching the limits dictated by photon and atom shot noise. Second, we foresee substantial innovative device engineering with a goal of improving the integration of the vapor cells with MEMS, photonic, and fiber-optic components. This is expected to lead to simpler, less expensive and more reliable devices more suited to large-scale manufacturing. Finally, we expect that even smaller magnetic sensors, with cell volumes approaching 10^{-9} cm^3 , will be developed that can be operated with extremely low power.

The technology appears highly promising for a broad range of applications. The potential for low-power operation of the sensors suggests that these devices will be very useful for remote detection of magnetic anomalies, where sensors can be deployed in remote locations

for long periods, and run on battery power. On the other hand, the potential for low-cost production may substantially benefit applications in biomagnetic instrumentation. Finally, the small size may be important for hand-held nuclear magnetic resonance systems for chemical identification.

References

- [1] V. Shah, S. Knappe, P. D. D. Schwindt, and J. Kitching, *Nature Photonics* **1**, 649 (2007).
- [2] *Magnetic Sensors – Emerging Technology Developments*, Frost & Sullivan, Document No. D08C (2006).
- [3] S. Knappe, V. Shah, P. D. D. Schwindt, L. Hollberg, J. Kitching, L. A. Liew, and J. Moreland, *Appl. Phys. Lett.* **85**, 1460 (2004).
- [4] D. Budker and M. Romalis, *Nature Physics* **3**, 227 (2007).
- [5] J. C. Allred, R. N. Lyman, T. W. Kornack, and M. V. Romalis, *Phys. Rev. Lett.* **89**, 130801 (2002).
- [6] W. Happer and H. Tang, *Phys. Rev. Lett.* **31**, 273 (1973).
- [7] W. Happer and A. C. Tam, *Phys. Rev. A* **16**, 1877 (1977).
- [8] H. G. Robinson, E. S. Ensberg, and H. G. Dehmelt, *Bull. Am. Phys. Soc.* **3**, 9 (1958).
- [9] M. V. Balabas, T. Karaulanov, M. P. Ledbetter, and D. Budker, *Phys. Rev. Lett.* **105**, 070801 (2010).
- [10] M. V. Balabas, D. Budker, J. Kitching, P. D. D. Schwindt, and J. E. Stalnaker, *J. Opt. Soc. Am. B* **23**, 1001 (2006).
- [11] W. Happer, *Rev. Mod. Phys.* **44**, 169 (1972).
- [12] J. Kitching, S. Knappe, and L. Hollberg, *Appl. Phys. Lett.* **81**, 553 (2002).
- [13] I. M. Savukov, S. J. Seltzer, and M. V. Romalis, *J. Magn. Reson.* **185**, 214 (2007).
- [14] P. D. D. Schwindt, B. Lindseth, S. Knappe, V. Shah, J. Kitching, and L.-A. Liew, *Appl. Phys. Lett.* **90**, 081102 (2007).
- [15] M. A. Perez, U. Nguyen, S. Knappe, E. A. Donley, J. Kitching, and A. M. Shkel, *Sens. Act. A* **154**, 295 (2009).
- [16] X. Song, H. F. Dong, and J. C. Fang, *4th IEEE International Conference on Nano/Micro Engineered and Molecular Systems* 231 (2009).
- [17] E. Hodby, E. Donley, and J. Kitching, *Appl. Phys. Lett.* **91**, 011109 (2007).
- [18] J. Clem, *IEEE Trans. Magn.* **23**, 1093 (1987).
- [19] T. Varpula and T. Poutanen, *J. Appl. Phys.* **55**, 4015 (1984).
- [20] S. K. Lee and M. V. Romalis, *J. Appl. Phys.* **103**, 084904 (2008).
- [21] W. C. Griffith, S. Knappe, and J. Kitching, *Opt. Exp.* **18**, 27167 (2010).
- [22] L. A. Liew, S. Knappe, J. Moreland, H. Robinson, L. Hollberg, and J. Kitching, *Appl. Phys. Lett.* **84**, 2694 (2004).
- [23] S. Knappe, in *Comprehensive Microsystems* **3**, edited by Y. Gianchandani, O. Tabata and H. Zappe (Elsevier B. V., Maryland Heights, MO, 2007), p. 571.
- [24] G. Wallis and D. I. Pomerantz, *J. Appl. Phys.* **40**, 3946 (1969).
- [25] S. Knappe, P. D. D. Schwindt, V. Shah, L. Hollberg, J. Kitching, L. Liew, and J. Moreland, *Opt. Exp.* **13**, 1249 (2005).
- [26] R. R. Mhaskar, S. Knappe, and J. Kitching, *IEEE International Frequency Control Symposium*, 376 (2010).
- [27] J. Preusser, V. Gerginov, S. Knappe, and J. Kitching, *IEEE Sensors Conference 2008*, Lecce, Italy, 344–346 (2008). <http://dx.doi.org/10.1109/ICSENS.2008.4716451>.

- [28] R. Lutwak, J. Deng, W. Riley, M. Varghese, J. Leblanc, G. Tepolt, M. Mescher, D. K. Serkland, K. M. Geib, and G. M. Peake, *36th Annual Precise Time and Time Interval (PTTI) Meeting, Washington, DC*, 339–354 (2004).
- [29] M. J. Mescher, R. Lutwak, and M. Varghese, *IEEE International Conference on Solid-State Sensors and Actuators*, Seoul, Korea, 311–316 (2005). <http://dx.doi.org/10.1109/SENSOR.2005.1496419>
- [30] D. W. Youngner, J. F. Detry, and J. D. Zook, United States Patent 6,900,702 (2005).
- [31] D. W. Youngner, L. M. Lust, D. R. Carlson, S. T. Lu, L. J. Forner, H. M. Chanhvongsak, and T. D. Stark, *Transducers/Eurosensors XXI*, U23 (2007).
- [32] M. A. Perez, S. Knappe, and J. Kitching, *IEEE Sensors Conference*, Waikoloa, Hawaii, 2155–2158 (2010). <http://dx.doi.org/10.1109/ICSENS.2010.5690546>
- [33] R. Wyllie, M. Kauer, G. S. Smetana, R. T. Wakai, and T. G. Walker, arXiv:1106.4779v1 (2011).
- [34] H. B. Dang, A. C. Maloof, and M. V. Romalis, *Appl. Phys. Lett.* **97**, 151110 (2010).
- [35] P. D. D. Schwindt, S. Knappe, V. Shah, L. Hollberg, J. Kitching, L. A. Liew, and J. Moreland, *Appl. Phys. Lett.* **85**, 6409 (2004).
- [36] A. L. Bloom, *Appl. Opt.* **1**, 61 (1962).
- [37] G. Bison, R. Wynands, and A. Weis, *Opt. Exp.* **11**, 904 (2003).
- [38] H. Xia, A. B. A. Baranga, D. Hoffman, and M. V. Romalis, *Appl. Phys. Lett.* **89**, 211104 (2006).
- [39] C. Johnson, P. D. D. Schwindt, and M. Weisend, *Appl. Phys. Lett.* **97**, 243703 (2010).
- [40] S. Knappe, T. H. Sander, O. Kosch, F. Wiekhorst, J. Kitching, and L. Trahms, *Appl. Phys. Lett.* **97**, 133703 (2010).
- [41] R. McDermott, S. K. Lee, B. ten Haken, A. H. Trabesinger, A. Pines, and J. Clarke, *Proc. Nat. Acad. Sci.* **101**, 7857 (2004).
- [42] V. V. Yashchuk, J. Granwehr, D. F. Kimball, S. M. Rochester, A. H. Trabesinger, J. T. Urban, D. Budker, and A. Pines, *Phys. Rev. Lett.* **93**, 160801 (2004).
- [43] J. A. Seeley, S. I. Han, and A. Pines, *J. Magn. Reson.* **167**, 282 (2004).
- [44] E. E. McDonnell, S. L. Han, C. Hilty, K. L. Pierce, and A. Pines, *Anal. Chem.* **77**, 8109 (2005).
- [45] M. P. Ledbetter, I. M. Savukov, D. Budker, V. Shah, S. Knappe, J. Kitching, D. J. Michalak, S. Xu, and A. Pines, *Proc. Nat. Acad. Sci.* **105**, 2286 (2008).
- [46] M. P. Ledbetter, C. W. Crawford, A. Pines, D. E. Wemmer, S. Knappe, J. Kitching, and D. Budker, *J. Magn. Reson.* **199**, 25 (2009).
- [47] T. Theis, P. Ganssle, G. Kervern, S. Knappe, J. Kitching, M. P. Ledbetter, D. Budker, and A. Pines, *Nature Physics* **7**, 571 (2011).
- [48] D. Maser, S. Pandey, H. Ring, M. P. Ledbetter, S. Knappe, J. Kitching, and D. Budker, *Rev. Sci. Instrum.* **82**, 086112 (2011).